Computational Condensed Matter 34 (2023) e00772

Contents lists available at ScienceDirect

Computational Condensed Matter

journal homepage: www.elsevier.com/locate/cocom

DFT study of cubic, tetragonal and trigonal structures of $KGeCl_3$ perovskites for photovoltaic applications

Mauwa .M Namisi [a,*], Robinson J. Musembi [a], Winfred M. Mulwa [b], Bernard O. Aduda [a,b]

[a] Department of Physics, University of Nairobi, P.O Box, 30197, Nairobi, Kenya
[b] Department of Physics, Egerton University, P.O Box 536-20115, Egerton, Kenya

ARTICLE INFO

Keywords:
DFT
Perovskites
All-inorganic
Photovoltaics
$KGeCl_3$

ABSTRACT

The study of suitable compounds for photovoltaic applications is one of the most fascinating research areas in the world. One of the less studied materials is $KGeCl_3$ and its potential is yet to be fully determined. Investigations of the structural, electronic, optical and mechanical properties of cubic, tetragonal and trigonal structures of pure inorganic $KGeCl_3$ perovskite have been done. All calculations have been performed using first-principle calculations based on density functional theory (DFT) in generalized gradient approximation with Perdew-Burke-Ernzerhof, PBE-GGA as the exchange correlation functional, as implemented in the Quantum ESPRESSO code. Further calculations using GW approximation have been performed on electronic band structures of the three phases of $KGeCl_3$ in order to validate the accuracy of GGA-PBE functional. The structural properties of the materials have been found to be consistent with previous observations in literature. All compounds have been found to display direct band gaps, with the top of the valence band (VB) dominated by Cl *2p* orbitals and the conduction band (CB) dominated by the Ge *2p* orbitals. The trigonal perovskite has been observed to have the largest band gap of 2.7 eV, with the cubic and tetragonal counterparts having 0.8 eV and 1.2 eV respectively. Calculated elastic constants, bulk and shear moduli have shown that the trigonal structure is mechanically unstable and brittle at ground state. Generally, the three phases of $KGeCl_3$ have been observed to possess a broad absorption spectrum covering the UV–Vis region and therefore making them suitable candidates for photovoltaic applications.

1. Introduction

Non-renewable energy sources such as fossil fuels are becoming increasingly scarce [1]. By 2040, the International Energy Agency (IEA) forecasts a growth of more than 25% in the energy demand [2]. The global energy demand compounded with the environmental risks associated with the use of non-renewable energies due to CO_2 emissions [3] have made it necessary to search for cleaner and more sustainable energies [2–5]. The switch to green energy can be greatly accelerated through search for complementary photovoltaic (PV) materials to supplement the already existing ones and perovskite [2] has been identified as one of the most promising materials. In recent years, perovskite structures have attracted interest mainly in photovoltaics due to their excellent properties such as high absorption coefficient, broad absorption spectrum, tunable band gap and low cost [6–8]. They have proven to be good candidates for diverse physical properties [9] because they consist of conductors, insulators, semiconductors and superconductors [10,11]. Perovskites are a class of compounds related to the natural-occurring mineral calcium titanate oxide ($CaTiO_3$) [12]. They have the general formula of ABX_3 where A and B are cations and X is a halogen. These structures have shown great improvement in their power conversion efficiency (PCE), faster than any other solar cell [13]. While silicon-based PV cells required 60 years to accomplish comparable PCE achievements (4%–29%), perovskite PV cells' PCE in creased from 3.8% (2009) [14–16] to 22.1% in 2016 [14–16] to 25.2% (2019) [17–19], to 26% PCE in 2020 [20]. Research into perovskite solar cells (PSCs) was initialized by hybrid organic inorganic perovskites of Methylammonium lead iodide ($MAPbI_3$, MA = CH_3NH_3). The solar cell was however short-lived because it was highly unstable due to the organic compounds' sensitivity to air, moisture and oxygen. The presence of lead also made it environmentally unsafe. This is because Pb^{2+} ions easily dissolve in water forming a toxic solution. Despite its potential in photovoltaics, these major drawbacks have stagnated perovskite photovoltaic commercialization. To counteract the harmful environmental issues

* Corresponding author.
E-mail address: namisimauwah@gmail.com (M..M Namisi).

https://doi.org/10.1016/j.cocom.2022.e00772
Received 25 August 2022; Received in revised form 21 October 2022; Accepted 21 November 2022
Available online 24 November 2022

due to Pb^{2+}, alternative replacement elements such as Ge^{2+} and Sn^{2+} have been previously proposed [19]. Use of inorganic elements in the A site like K^{2++} and Rb^{2+} have also been found to improve the stability of perovskites. Recently, germanium-based perovskites have been studied by Refs. [13,19,21] for optoelectronic applications. In these studies, $KGeX_3$ and $RbGeX_{33}$ (X = Cl, Br) were found to be perfect candidates for solar cell applications and optoelectronics due to their high absorption coefficient, low reflectivity and high static refractive index [13]. Currently, perovskites with the best PCE are the lead-based organic-inorganic types [22]. The desire to have stable less toxic perovskite solar cells then prompts researchers to pursue relentlessly for a suitable and equally well performing inorganic lead-free perovskites absorber with PCEs either matching or surpassing the current devices. The structurally ideal perovskite exists in the cubic phase [12,23–25]. They also exist in lowered symmetries such as the orthorhombic, trigonal, tetragonal and monoclinic structures. The perovskite structures are dependent on the Goldschmidt tolerance factor (GTF) [25] τ as given in Equation (1).

$$\tau = \frac{r_A + r_X}{\sqrt{2}(r_B + r_X)} \tag{1}$$

where r_A, r_B and r_X are ionic radii of cations A, B and halide X respectively.

These distorted perovskites emerge from the decomposition of unstable perovskite structures to make them more energetically stable. Perovskite distortion is mainly due to the BX_6 octahedron tilting and occurs when the atomic sizes vary. From the GTF, perovskites with $\tau = 1$ exists in the cubic phase and are structurally ideal. On the other hand, when $\tau > 1$, perovskites have the corner-sharing octahedra bulging outwards, this happens when the A cation is too big, making the BX_6 octahedron link to be broken. Furthermore, when the A cation is too small in relation to the octahedra, then the octahedra tilts inwards since the A cation is not able to touch its neighbours therefore making $\tau < 1$. DFT formalism has been employed to investigate the cubic $KGeCl_3$ perovskite [26,27]. The effects of structural distortions of $KGeCl_3$, however, remain unexplored. This section is critical because the change in the structural composition of perovskites have been found to alter the macroscopic and microscopic properties of the compound and its applications such as optoelectronic [28] and photovoltaic [29]. This study aims to contribute to this domain by conducting an in-depth study on the effect of structural distortions in the photovoltaic properties of inorganic lead free $KGeCl_3$ perovskite. The tetragonal, cubic and trigonal structures of $KGeCl_3$ have been studied by investigating their structural, electronic, optical and mechanical properties using GGA-PBE approximations. The properties of the distorted tetragonal and trigonal perovskites are then compared to the structurally ideal cubic perovskite, mainly to check if these distorted perovskites have potential in photovoltaics as their cubic counterparts. The GW approximation was employed to confirm the electronic band structure findings from the use of GGA-PBE functional. This study also aims at shedding light on elastic properties of tetragonal and trigonal $KGeCl_3$ compounds which to the best of our knowledge remains unexplored neither experimentally nor computationally. Furthermore, no previous work has been reported on the structural properties of the tetragonal *P4mbm* and trigonal *R3c* structures.

2. Computational details

Ab initio calculations were done within the DFT formalism as implemented in the Quantum ESPRESSO (QE) code [30]. The self consistent calculations were performed to solve the Kohn- Sham equations [31] in Generalized Gradient Approximation using Perdew-Burke-Ernzerhof (GGA-PBE) [32] as the exchange correlational functional. The cubic, tetragonal and trigonal perovskites belong to the *Pm3 m*, *P4mbm* and *R3c* space groups with $\alpha = \beta = \gamma = 90^o$; a = b = c = 5.89 Å, $\alpha = \beta = \gamma = 90^o$; a = b = 7.97 Å ≠ c = 5.81 Å and $\alpha = \beta = \gamma = 60.04^0$; a = b = c = 7.67 Å, respectively. The unit cell for the cubic *Pm3 m* $KGeCl_3$ has 5 atoms, that is, 1 K atom, 1 Ge atom and 3 Cl atoms. The K atoms are located at the corner positions with fractional co-ordinates of (0, 0, 0). The Ge is located at the body-centered positions at (0.5, 0.5, 0.5), while the Cl atoms occupy the face centered positions at (0.5, 0.5, 0), (0, 0.5, 0) and (0.5, 0, 0.5). The $KGeCl_3$ tetragonal (*P4mbm*) perovskite unit cell has 10 atoms, that is, 2 K atoms, 2Ge atoms and 6 Cl atoms. The Ge atoms are located at the corner and at the base centered positions with fractional coordinates of (0, 0, 0) and (0.5, 0.5, 0). The Cl atoms occupy the face centered positions around the germanium atoms. Fig. 1 shows the visual representation of the three phases of $KGeCl_3$ investigated in this study.

Structural optimization was carried out to ensure accuracy in the results. *K*-points convergence was done from 2 × 2 × 2 to 24 × 24 × 24 at intervals of 2 × 2 × 2. The kinetic energy cut-off (ecut) convergence was carried out in the range from 10 to 125 Ry at intervals of 5Ry. Lattice constant optimization was then carried out using the converged values of the *k*-points and the cut-off energy. Convergence was achieved for all the materials with the convergence criterion set at 10^{-4} Ry. The *K*-point sampling of the Brillouin zone was done using the Monkhorst and Pack scheme [33] with the *K*-points set at 8 × 8 × 8 grids. Electronic band structure calculations were executed using the GGA-PBE and the GW approximations. This comparative study was done because GGA-PBE is known to underestimate electronic band gaps of materials. THERMO-PW technique [34,35] was employed in the calculation of the mechanical properties, that is, the elastic constants, bulk and the shear moduli. THERMO-PW was also used to calculate the real and imaginary part of the dielectric function.

3. Results and discussions

3.1. Structural properties

The GTF for the materials was calculated to determine the type of octahedron tilting. The cubic $KGeCl_3$ had $\tau = 1$, ascertaining that it is the ideal structure. The tetragonal $KGeCl_3$ had $\tau < 1$, hence the $GeCl_3$ would tilt inwards to ensure the corner-sharing link is not broken. For the trigonal structures, $KGeCl_3$ had $\tau > 1$ making the $GeCl_3$ octahedra bulge outwards causing the distortion. The cut-off energy and *K*-point convergence were achieved at 100Ry and 8 × 8 × 8 respectively. The optimized values of the *k*-points, ecut and lattice constant *a* are shown in Figs. 2–4 respectively. The obtained lattice constant values are presented in Table 1 and were found to corroborate previous literature values for the cubic structures. The equilibrium volume V_0, bulk modulus *B* and its pressure derivative B^l was obtained by fitting the total energies against the calculated lattice constants into the Murnaghan equation of states (MEoS) [36,37] as given in equation (2), in order to extract the physical properties such as the bulk modulus, its pressure derivative and the equilibrium volumes.

$$E(V) = \frac{B_0 V}{B_0^1}\left[\left(\frac{V_0}{V}\right)^{B_0^1}\frac{1}{B_0^1 - 1} + I\right] + \text{Constant} \tag{2}$$

3.2. Electronic properties

The electronic properties were studied by calculating the electronic band structures and the density of states (DOS). Figs. 5 and 6 show the band structure plots obtained from the PBE-GGA and GW approximation. The *k* point mesh for the electronic band structure calculations was increased to a denser *k*-point mesh by sampling the high symmetry points in the first Brillouin zone. The *k*-point sampling is unique to each structure type [39]. The *k*-paths used for the calculations are $\Gamma - X - M - \Gamma - R - X|M - R$ for the cubic, $\Gamma - X - M - \Gamma - Z - R - A - Z|X - R|M - A$ for the tetragonal and $\Gamma - L - B_1 B - Z - \Gamma - X|Q - F - P_1 - Z|L - P$ for

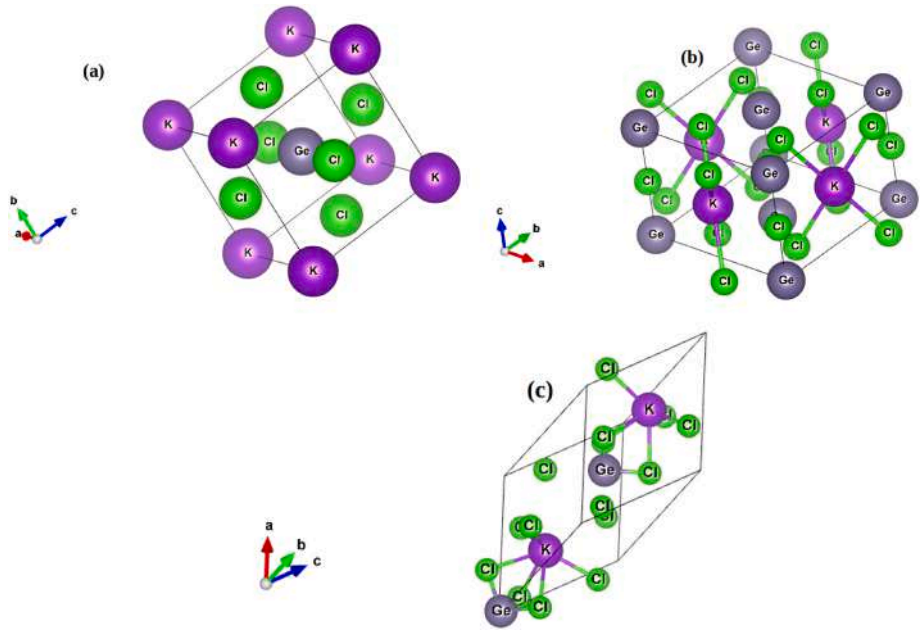

Fig. 1. Schematic representation of the (a) cubic, (b) tetragonal and (c) trigonal $KGeCl_3$ perovskites using the VESTA package [38].

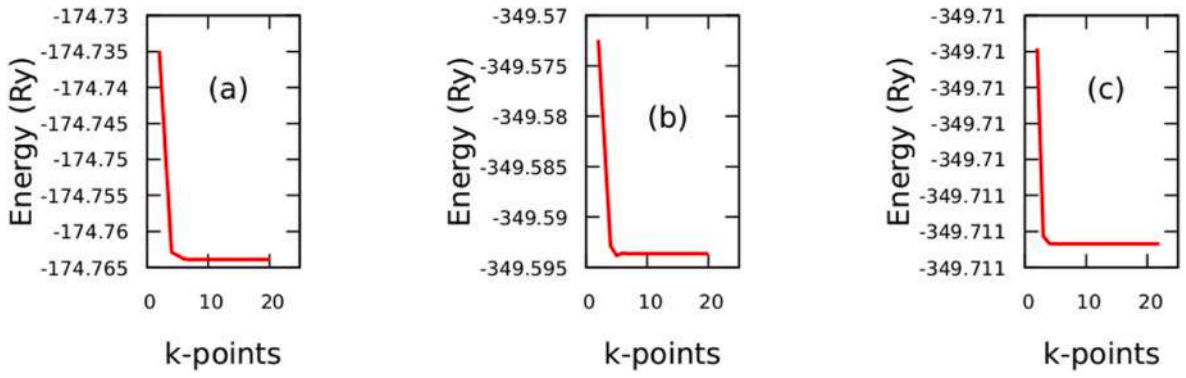

Fig. 2. The *k*-point mesh as a function of total energy (Ry) of the (a) cubic, (b) tetragonal and (c) trigonal $KGeCl_3$ perovskite materials.

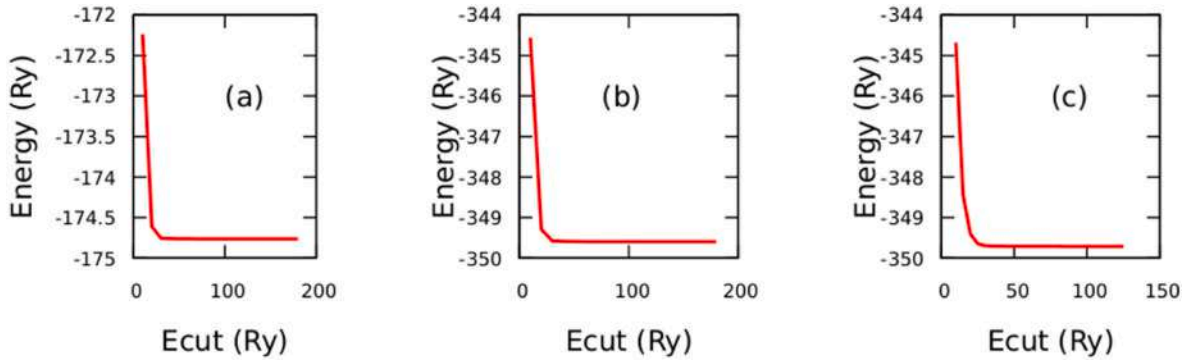

Fig. 3. The cut-off energy (Ecut) as a function of total energy (Ry) for the (a) cubic, (b) tetragonal and (c) trigonal $KGeCl_3$ perovskite materials.

the trigonal structures respectively. All the three structures of the compound were found to exhibit a direct band gap with a semiconductor characteristic. The cubic $KGeCl_3$ had the CB minimum and VB maximum located at point *R*. The tetragonal $KGeCl_3$ had the CB minimum and VB maximum located at points *Z* and *Z*|*X*. The trigonal $KGeCl_3$ had the CB minimum and VB maximum located at points *Z* and *X*|*Q*. For confirmation of electronic band structure results from the GGA-PBE functional, GW approximation was utilized. Fig. 6 shows the band structure obtained from GW approximations. The calculated band gaps in eV using the GGA-PBE and GW approximations are given in Table 2. The density of states (DOS) calculation is relevant in studying the detailed electronic band structure of materials [40]. The partial density of states (PDOS) of $KGeCl_3$ perovskites are shown in Fig. 5. For all the phases, the VB is dominated by the *2p* orbital of the Cl halogen. The CB is

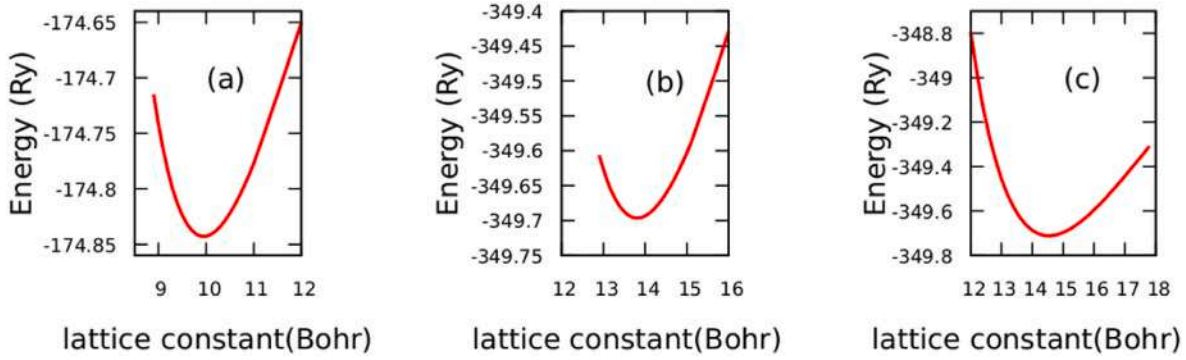

Fig. 4. The lattice constant a as a function of total energy (Ry) of the (a) cubic, (b) tetragonal and (c) trigonal $KGeCl_3$ perovskite materials.

Table 1
The optimized lattice constants a in Å compared with the previous work, the GTF (τ), the equilibrium volumes in $Å^3$, minimum energy in Ry, bulk modulus B in GPa and its derivatives obtained from the MEoS for the $KGeCl_3$ compounds.

Material	a (Å)	a (Å)(Previous Work)	V_0	B (GPa)	B^I	Minimum energy	τ
$KGeCl_3$ Cubic	5.269	5.570 [27], 5.290 [26]	145.010	25.800	4.590	−174.843	1.003
$KGeCl_3$ Tetragonal	7.302	—	284.470	27.800	4.410	−349.696	0.957
$KGeCl_3$ Trigonal	7.634	—	326.330	20.700	4.040	−349.711	1.069

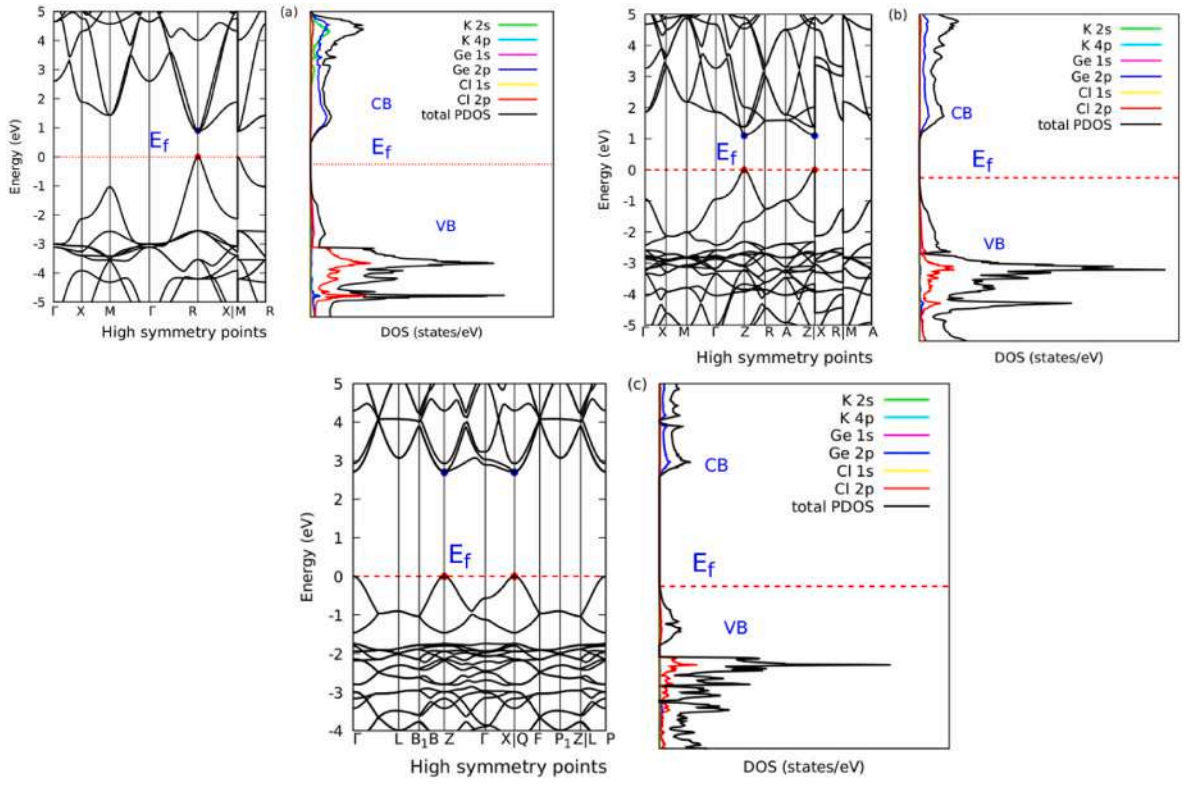

Fig. 5. The electronic band structures and density of states of (a) cubic, (b) tetragonal and (c) trigonal $KGeCl_3$ perovskites using DFT-(GGA-PBE) approximation. The Fermi energy level is shown by the horizontal red dashed line. VB maximum and CB minimum are shown by the red and blue circles respectively. (For interpretation of the references to colour in this figure legend, the reader is referred to the Web version of this article.)

dominated by the *2p* orbital of the Ge atoms. The K atoms do not contribute much to the PDOS.

3.3. Mechanical properties

Understanding the mechanical stability of materials is crucial in materials engineering. The elasticity of a material explains how it deforms under strain before rebounding to its original nature when the load is removed [19]. The mechanical properties calculated are the elastic constants, bulk and shear moduli, Cauchy pressure, anisotropy, machinability, hardness and Poisson's ratio. Elastic constants of materials are important in determining the crystals' response to external forces and the strength of materials. The Cauchy pressure, Poisson and Pugh's ratio are extremely accurate and powerful in classifying

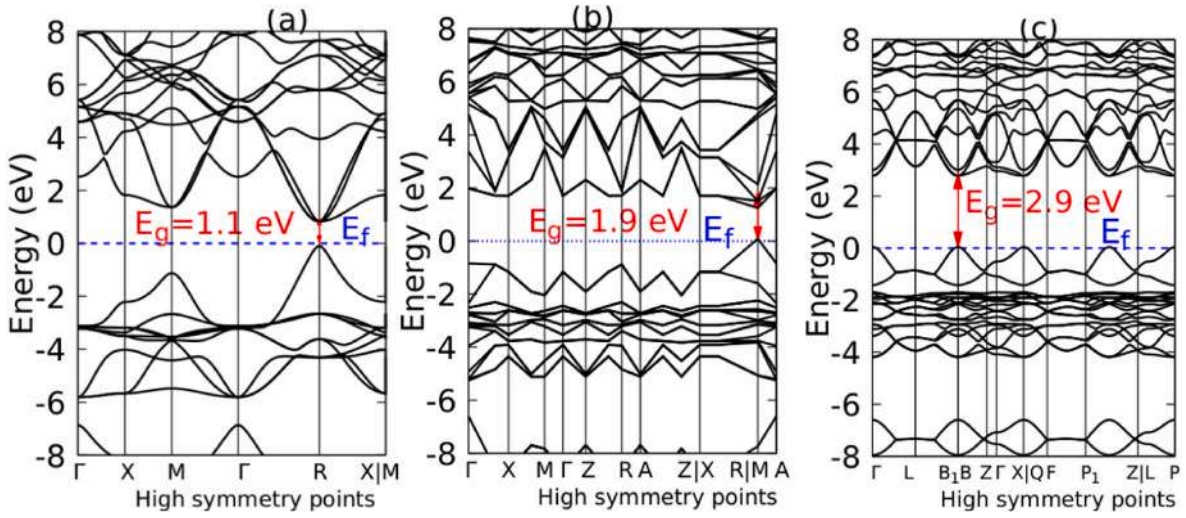

Fig. 6. The electronic band structures of (a) cubic, (b) tetragonal and (c) trigonal phases of $KGeCl_3$ perovskites using GW approximation.

Table 2
Band gap values for $KGeCl_3$ in eV calculated using GGA-PBE and GW approximations and compared with previous work where applicable.

Material	GGA-PBE	GW	Previous Work
$KGeCl_3$ Cubic	0.800	1.1	0.900 [27], 0.958 [26]
$KGeCl_3$ Tetragonal	1.200	1.9	—
$KGeCl_3$ Trigonal	2.700	2.9	—

materials as either ductile or brittle [10]. Mechanical property calculations were done using THERMO-PW as a post-process in QE. The results obtained for the cubic phase were compared to previous literature [27]. The mechanical stability is confirmed from the elastic constants using the Born stability criteria [41]. The cubic phase has only three independent elastic constants and the necessary stability conditions are given by Equations (3)-5)

$$C_{11} - C_{12} > 0\,, \tag{3}$$

$$C_{11} + 2C_{12} > 0\,, \tag{4}$$

$$C_{44} > 0 \tag{5}$$

The tetragonal structures have six independent elastic constants and are mechanically stable if they satisfy Equations (6)-8)

$$C_{11} > |C_{12}|\,, \tag{6}$$

$$2C_{13}^2 < C_{33}(C_{11} + C_{12})\,, \tag{7}$$

$$C_{44} > 0, \tag{8}$$

The trigonal structures have seven independent elastic constants and are stable if Equations (9)–(12) are obeyed.

$$C_{11} > |C_{12}|\,, \tag{9}$$

$$C_{44} > 0\,, C_{33} > 0\,, C_{11} > 0 \tag{10}$$

$$C_{13}^2 < \frac{1}{2}C_{33}\,(C_{11} + C_{12}) \tag{11}$$

$$\left[(C_{11} - C_{12})\,C_{44} - 2C_{14}^2\right] > 0 \equiv C_{44}C_{66} \tag{12}$$

The bulk and shear moduli can be approximated using either the Voigt [42,43] or the Reuss [44,45] theories and their averages are calculated using the Hill [46] averaging scheme. From the Voigt theory, the bulk B_V and shear G_V moduli are estimated by Equations (13) and (14).

$$B_V = \frac{1}{9}[(C_{11} + C_{22} + C_{33}) + 2(C_{12} + C_{23} + C_{31})] \tag{13}$$

$$G_V = \frac{1}{15}[(C_{11} + C_{22} + C_{33}) - (C_{12} + C_{23} + C_{31}) + 3(C_{44} + C_{55} + C_{66})] \tag{14}$$

From the Reuss scheme, the bulk B_R and shear G_R moduli are determined by Equations (15) and (16).

$$\frac{1}{B_R} = (S_{11} + S_{22} + S_{33}) + 2(S_{12} + S_{23} + S_{31}) \tag{15}$$

$$\frac{15}{G_R} = 4(S_{11} + S_{22} + S_{33}) - 4(S_{12} + S_{23} + S_{31}) + 3(S_{44} + S_{55} + S_{66}) \tag{16}$$

The averages of the bulk B_H and the shear G_H moduli, from the two schemes are addressed by Equations (17) and (18).

$$B_H = \frac{B_V + B_R}{2} \tag{17}$$

$$G_H = \frac{G_V + G_R}{2} \tag{18}$$

The brittleness of the materials was checked using the Pugh criteria [47] where the ratio of the bulk to the shear modulus is related to the critical value of 1.75. Materials with $\frac{B}{G} > 1.75$ are ductile and those with ratios less than the critical value are considered brittle [48]. The Poisson's ratio ν and the Young's modulus E_H were obtained from the bulk and shear moduli using the Equations (19) and (20).

$$\nu = \frac{3B_H - 2G_H}{2(3B_H + G_H)} \tag{19}$$

$$E_H = \frac{9B_H G_H}{(3B_H + G_H)} \tag{20}$$

The Zener's (A_Z) and shear anisotropic factors (A_1, A_{22} A_3,), can be used to calculate the degree of anisotropy in the bonding between atoms in different planes. A_1 is in the {100} planes between the <011> and <010> directions, A_2 is in the {010} planes between the <101> and <001> directions and A_3 is in the {001} planes between the <110> and <010> directions. A_1, A_{22} A_3, and A_Z are approximated by the relations in equations (21)–(24) respectively. Crystals with A_1, A_{22} A_3 , $A_{ZZ} = 1$ are isotropic while anisotropic materials have A_1, A_{22} A_3 , $A_Z \neq 1$. Any deviation from unity gives the materials' degree of anisotropy.

$$A_1 = \frac{4C_{44}}{C_{11} + C_{33} - 2C_{13}} \tag{21}$$

$$A_2 = \frac{4C_{55}}{C_{22} + C_{33} - 2C_{23}} \tag{22}$$

$$A_3 = \frac{4C_{66}}{C_{11} + C_{22} - 2C_{12}} \tag{23}$$

$$A_Z = \frac{2C_{44}}{C_{11} - C_{12}} \tag{24}$$

Hardness of the three materials was calculated using Vickers hardness [49] using equation (25).

$$H_V = \frac{(1-2\nu)E_H}{6(1+\nu)} \tag{25}$$

The machinability index ($\frac{B}{C_{44}}$) [50] is a criterion used to measure material hardness. It indicates how easy a material can be cut and machined during engineering processes. Materials with a high machinability index are hard, not easy to cut through hence would require more time to produce finely finished surfaces.

From the calculations, elastic constants for the cubic and tetragonal structures are positive and satisfy the Born stability criteria indicating mechanical stability. The $KGeCl_3$ trigonal phase, however, does not satisfy $C_{11} > C_{12}$ and has a negative value of C_{12}. This shows that the trigonal perovskite structure is mechanically unstable. The unidirectional elastic constant C_{11} relates to the unidirectional compression in the main crystallographic directions. For the cubic and tetragonal structures, $C_{11} > C_{44}$ demonstrating that the two have lower resistance to pure shear deformation than the unidirectional compressive strength. Table 3 shows the calculated values of the elastic constants C_{ij}'s. The Cauchy Pressure is given by $(C_{12} - C_{44})$ [19]. Materials with a positive value of the Cauchy pressure are ductile and brittle otherwise. From the Poisson's ratio, materials with $\nu > 0.26$ are ductile while those with $\nu < 0.26$ are brittle. The Pugh's criterion, Cauchy pressure and Poisson's ratio are all consistent in identifying the ductility of the cubic and tetragonal materials and the high brittle nature of the trigonal perovskite. The tetragonal perovskite, however, is more ductile than its cubic counterpart.

The Poisson's ratio, machinability, hardness, Young's modulus, $\frac{B}{G}$, bulk and shear moduli from the Voigt, Reuss and Hill approximations are listed in Table 4. The bulk and shear moduli are used to determine the compressibility of materials. They reduce from tetragonal-cubic-trigonal with the trigonal structures having the lowest moduli. This indicates that the stiffness of the material increases as the perovskite symmetry lowers.

From the $\frac{B}{G}$ ratio, the cubic and tetragonal perovskite phases are ductile since they satisfy $\frac{B}{G} > 1.75$. The trigonal structure has $\frac{B}{G} = -0.326 < 1.75$ hence is very brittle implying that it would crack easily under mechanical forces. The cubic and tetragonal structures also have bulk moduli that are consistent with the MEoS calculations. From the Young's modulus, E_H, the cubic and tetragonal structures are stiffer compared to the trigonal structure which is more elastic. This then makes the trigonal perovskite phase undergo deformations more drastically under mechanical forces. The tetragonal perovskite has lower machinability index compared to the cubic perovskite showing that it is easier to manipulate in machinery processes. The trigonal phase has a negative machinability index. The Vickers hardness (H_V) predicts that the trigonal structure is extremely hard compared to the cubic and tetragonal perovskites. This then shows that it would be time-consuming to cut through and polish its surfaces. For photovoltaic applications, the trigonal perovskite would be ineffective. The obtained shear and Zener's anisotropy factors A_1, A_{22} A_3 , A_Z are illustrated in Table 5.

The calculations indicate that $KGeCl_3$ is anisotropic in all the three phases. The cubic phase has equal shear and Zener anisotropy indices. For A_1 , A_2 and A_Z, the degree of anisotropy increases from trigonal-cubic-tetragonal. This shows that the tetragonal structure exhibits more anisotropy within the crystallographic planes. The trigonal structure has negative values of anisotropy. In A_Z , the degree of anisotropy increases from cubic-trigonal-tetragonal, the tetragonal structures having the highest index.

3.4. Optical properties

It is important to investigate the optical properties of a photovoltaic application candidate. Frequency response to energy of incident photon ($E = h\nu$) of distinct optical parameters of a compound is described using optical properties of that compound [51]. Fig. 7(a–f) shows graphs of the optical properties against the energy in eV. Frequency dependent complex dielectric function, $\mathscr{E}(\omega)$, is employed in determining distinct optical parameters of any compound [51]. The Complex dielectric function is determined by the relation in Equation (26).

$$\mathscr{E} = \varepsilon_1(\omega) + i\varepsilon_2(\omega) \tag{26}$$

where ε_1 is the real part and ε_2 the imaginary part of the complex dielectric function. The optical properties were studied as a function of the energy in eV. The other optical properties such as reflectivity, absorption coefficient, energy loss, exciton and refractive indices can be obtained from the complex dielectric function. The absorption coefficient $\alpha(\omega)$ is calculated from ε_1 and ε_2 using Equation (27).

$$\alpha(\omega) = \sqrt{2}\omega\left(\sqrt{\varepsilon_1^2(\omega) + \varepsilon_2^2(\omega)} - \varepsilon_1(\omega)\right)^{\frac{1}{2}} \tag{27}$$

The refractive index is estimated by Equation (28).

$$n(\omega) = \left(\frac{\sqrt{\varepsilon_1^2(\omega) + \varepsilon_2^2(\omega)} + \varepsilon_1(\omega)}{2}\right)^{\frac{1}{2}} \tag{28}$$

The energy loss, L(ω) is given by Equation (29).

$$L(\omega) = \frac{\varepsilon_2(\omega)}{\varepsilon_1^2(\omega) + \varepsilon_2^2(\omega)} \tag{29}$$

The reflectivity, R(ω) is addressed by Equation (30).

$$R(\omega) = \frac{(n-1)^2 + K^2}{(n+1)^2 + K^2} \tag{30}$$

The optical properties were calculated in the energy range of 0–20eV. The relation between the energy in eV and the wavelength in nm is illustrated by Equation (31).

$$\lambda = \frac{hc}{e} \tag{31}$$

Table 3
The calculated elastic constants, C_{ij} 's and the Cauchy pressure of the $KGeCl_3$ materials in GPa using GGA-PBE approximation.

Material	C_{11}	C_{12}	C_{13}	C_{22}	C_{23}	C_{33}	C_{44}	C_{55}	C_{66}	$C_{12} - C_{44}$
$KGeCl_3$ Cubic	56.166	9.119	9.119	56.166	9.119	56.166	8.340	8.340	8.340	0.779
Other calc [27].	56.74	11.19	11.19	56.74	11.19	56.74	7.77	7.77	7.77	3.420
$KGeCl_3$ Tetragonal	43.845	25.029	14.084	43.845	14.084	60.639	10.590	10.590	22.296	14.439
$KGeCl_3$ Trigonal	2.059	−5.536	1.519	2.059	1.519	−0.891	5.991	5.991	3.797	−11.527

Table 4

The bulk and shear moduli in GPa under the Voigt, Reuss and Hill approximations, the Pugh's $\frac{B}{G}$ ratio, Young's modulus (E_H), Cauchy pressure and Poisson's ratio (v) of the $KGeCl_3$ materials derived from the elastic constants.

Material	BV	BR	BH	GV	GR	GH	BG	v	E_H	B/C44	HV
$KGeCl_3$ Cubic	24.801	24.801	24.801	14.413	11.242	12.828	1.933	0.279	32.825	2.974	1.886
Other calc [27].	–	–	26.370	–	–	12.17	2.17	0.3	31.64	3.393	1.623
$KGeCl_3$ Tetragonal	28.303	28.258	28.280	15.037	12.990	14.014	2.018	0.287	36.082	2.671	1.987
$KGeCl_3$ Trigonal	−0.196	−1.742	−0.969	3.537	2.412	2.975	−0.326	−0.049	5.657	−0.162	130.156

Table 5

The calculated shear anisotropic factors (A_1, A_{22} A_3 , A_Z) for the cubic, tetragonal and trigonal $KGeCl_3$ perovskites.

Material	A1	A2	A3	AZ
$KGeCl_3$ Cubic	0.354	0.354	0.354	0.354
Other calc [27].	–	–	–	0.340
$KGeCl_3$ Tetragonal	0.555	0.555	2.370	1.126
$KGeCl_3$ Trigonal	−12.813	−12.813	0.990	1.578

From Fig. 7(a), $\varepsilon_1(0)$, the electronic part of the static dielectric function, is 3.82, 5.18 and 6.56 for the trigonal, tetragonal and cubic $KGeCl_3$ phases respectively. Refractive indices can be calculated from these square roots of the static values [51] and they are presented in Table 6. This shows that $\varepsilon_1(0)$ increases as the structure becomes more ideal. The imaginary spectrum is crucial because it relates to the band structure of materials [52,53]. From the Fig. 7(b) of ε_2 as a function of the energy in eV, the critical onset points are at 0.990, 2.748 and 1.137 for the cubic, trigonal and tetragonal phases respectively. These points are closely comparable to the calculated band gaps of the structures. From Fig. 7(c), the highest reflectivity peaks were found at low energy zones, that is, 2.5eV–3.0eV.

Reflectivity decreased as photon energy increased. The energy loss $L(\omega)$ depicts the energy lost by an electron as it propagates through the system. From the graph of energy loss as a function of energy in Fig. 7 (d), the energy loss is gradual and low from 0 to 5eV after which the energy losses increase. This shows that in the visible region, all the materials retain most of their energy and only a small amount is lost to the environment. From Fig. 7(e), $KGeCl_3$ has a broad absorption spectrum from 2.5eV to 16eV which is within the UV–Vis zones. This confirms that the investigated compounds are suitable candidates for photovoltaic applications. The refractive index is the measure of the bending of light. The cubic structures have the highest refractive indices with the trigonal structures having the lowest showing that $n(\omega)$ decreases as the perovskite distorts to lower symmetries. The static refractive indices, $n(0)$ are located at 2.551, 1.966 and 2.280 for the cubic, trigonal and tetragonal structures respectively. From this, it was noted that $n(0)$ decreased from cubic-tetragonal-trigonal, that is, as the perovskite shifted away from the ideal structure.

4. Conclusion

In this study, we have investigated the stability and suitability of the three phases of $KGeCl_3$ for photovoltaic applications. The structural, electronic, elastic and optical properties of all-inorganic $KGeCl_3$ perovskites have been investigated. The compounds were found to have

Table 6

The refractive indices for the $KGeCl_3$ materials.

Material	$n(\omega)$
$KGeCl_3$ Trigonal	1.926
$KGeCl_3$ Cubic	2.585
$KGeCl_3$Tetragonal	2.279

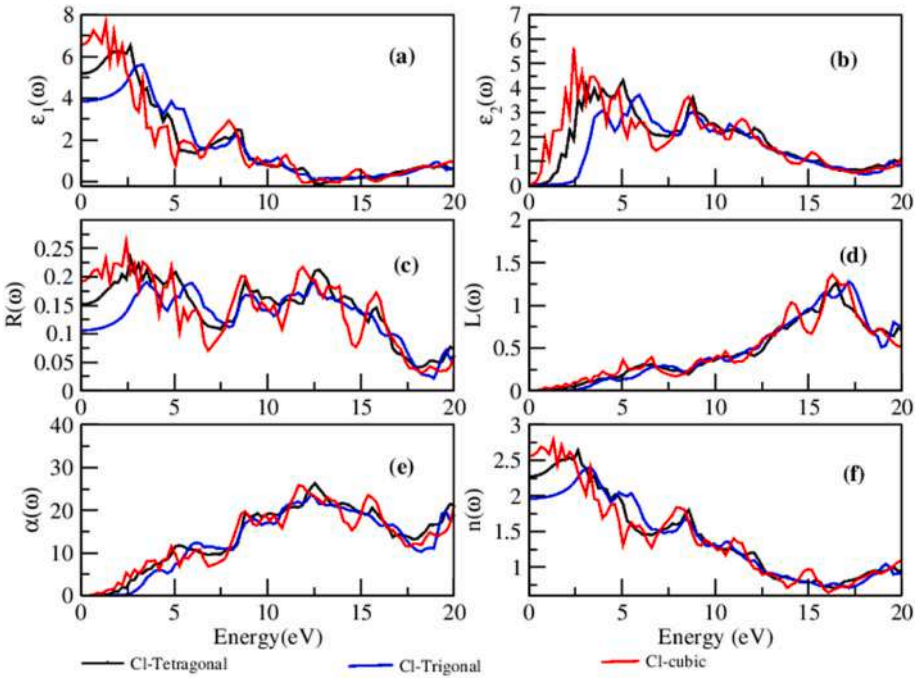

Fig. 7. The (a) real part and (b) imaginary part of the dielectric constant, (c) reflectivity, (d) energy loss, (e) absorption coefficient and (f) refractive index as a function of the energy in eV for the three $KGeCl_3$ perovskite materials.

reliable structural stability with lattice constants of 5.269 Å, 7.302 Å and 7.634 Å for cubic, tetragonal and trigonal phases respectively at ground state. Direct band gaps of 2.7eV, 0.8eV and 1.2eV were obtained for the trigonal, cubic and tetragonal phases respectively. GW approximation was also employed alongside GGA-PBE to calculate the electronic band gaps. GW approximation resulted to electronic band gap values of 2.9eV, 1.1eV and 1.9eV for the trigonal, cubic and tetragonal structures respectively. Electron transition contribution in the valence band for the three phases was mainly by Cl_*2p* orbitals. The calculated elastic constants established the required conditions for elastic stability, confirming mechanical stability in tetragonal and cubic phases while the trigonal phase was mechanically unstable and brittle. Optical absorption onsets were realized at 0.990eV, 2.748eV and 1.137eV for cubic, trigonal and tetragonal phases respectively. This trend reveals that narrow absorption onsets have higher $\varepsilon_2(\omega)$. From Fig. 7(e), there is absorption of photon energy in the UV–Vis zones of electromagnetic spectrum therefore suitable candidates for photovoltaic applications. From the property calculations, the cubic and tetragonal structures showed consistency in potentiality in photovoltaic applications.

Funding statement

This work would not have been possible without the support from the International Science Program, ISP, (KEN02) ([Grant 500-661-127], PI- Prof. Aduda Bernard O.) for the fees and research grant. This is through the condensed matter thematic group of the Department of Physics, University of Nairobi.

Declaration of competing interest

The authors declare that they have no known competing financial interests or personal relationships that could have appeared to influence the work reported in this paper.

Data availability

Data will be made available on request.

Acknowledgements

Much appreciation to the Centre of High-Performance Computing (CHPC) in Cape Town, South Africa for providing the computational resources used in this work, through the project MATS1321. This work was carried out with the aid of a grant from UNESCO and the International Development Research Centre, Ottawa, Canada. The views expressed herein do not necessarily represent those of UNESCO, IDRC or its Board of Governors.

References

[1] I. Hamideddine, H. Jebari, N. Tahiri, O. El Bounagui, H. Ez-Zahraouy, The investigation of the electronic, op tical, and thermoelectric properties of the Ge-based halide perovskite $AGeI_2Br$ (A=K, Rb, Cs) compound for a photovoltaic application: first principles calculations, Int. J. Energy Res. (2022) 1–11.
[2] D. Kevin, G. Giulia, Dealing with lead in hybrid perovskite: a challenge to tackle for a bright future of this technology? Adv. Energy Mater. (2020), 2001471.
[3] R. Mohammad Abdur, M. Saiduzzaman, B. Arpon, M.H. Khandaker, First-principles calculations to explore the metallic behavior of semiconducting lead-free halide perovskites $RbSnX_3$ (X = Cl, Br) under pressure, European Physical Journal Plus 137 (6) (2022).
[4] W. Rui, M. Muhammad, D. Yu, W. Zhao-Kui, X. Jingjing, Y. Yang, A review of perovskites solar cell stability, Adv. Funct. Mater. 29 (47) (2019) 1–25.
[5] V. Nikolaos F, Photovoltaic technology and innovative solar cells, EJECE,Eur. J. Electr. Comput. Eng. 2 (1) (2018) 1–7.
[6] M. Roknuzzaman, K.K. Ostrikov, K. Chandula Wasalathi lake, C. Yan, H. Wang, T. Tesfamichael, Insight into lead-free organic-inorganic hybrid perovskites for photovoltaics and optoelectronics: a first-principles study, Org. Electron. 59 (2018) 99–106.
[7] K. Sabine, M.A.L. Miguel, B. Silvana, Stability and electronic properties of new inorganic perovskites from high-throughput *ab initio* calculations, J. Mater. Chem. C 4 (15) (2016) 3157–3167.
[8] I. Hamideddine, H. Zitouni, N. Tahiri, O. El Bounagui, H. Ez-Zahraouy, A DFT study of the electronic structure, optical, and thermoelectric properties of halide perovskite $KGeI_{3-x}Br_x$ materials: photovoltaic applications, Appl. Phys. A 127 (6) (2021) 1–11, 11.
[9] H. Muhtasim Ali, Md S, A. Tariqul Islam, S. Ismile Khan, M.H. Khandaker, Ultraviolet to visible band gap engineering of cubic halide $KCaCl_3$ perovskite under pressure for optoelectronic applications: insights from DFT, Royal Society of Chemistry 11 (2021).
[10] M. Md Riaz, M. Saiduzzaman, A. Tariqul Islam, D. Wasif Abu, M.H. Khandaker, Electronic phase transition from semiconducting to metallic in cubic halide $CsYbCl_3$ perovskite under hydrostatic pressure, Physica B: Phys. Condens. Matter 630 (2022).
[11] S. Ismile Khan, Md S, A. Tariqul Islam, H. Muhtasim Ali, M.H. Khandaker, Band gap shifting of halide perovskites $CsCaBr_3$ from ultraviolet to visible region under pressure for photovoltaic applications, Mater. Sci. Eng. B 278 (2022).
[12] T. Richard, Perovskites structure–property relationships, John Wiley Sons, ltd 1 (1) (2016) xi–3.
[13] S.K. Mitro, M. Saiduzzaman, A. Tariqul Islam, M.H. Khandaker, Band gap engineering to stimulate the optoelectronic performance of lead-free halide perovskites $RbGeX_3$ (X = Cl, Br) under pressure, J. Mater. Sci. 33 (2022).
[14] G. Feliciano, H.J. Snaith, Toward lead-free perovskite solar cells): first-principles calculations, ACS Energy Lett. 1 (6) (2016) 1233–1240.
[15] K. Akihiro, T. Kenjiro, S. Yasuo, M. Tsutomu, Organometal halide perovskites as visible-light sensitizers for photovoltaic cells, J. Am. Chem. Soc. 131 (17) (2009) 6050–6051.
[16] S. Michael, M. Taisuke, S. Ji-Youn, D. Konrad, C.-B. Juan Pablo, N. Mohammad, Khaja, M.Z. Shaik, T. Wolfgang, A. Antonio, H. Anders, G. Michael, Cesium-containing triple cation perovskite solar cells: improved stability, reproducibility and high efficiency, Energy Environ. Sci. 9 (6) (2016) 1989–1997.
[17] Y.K. Jin, L. Jin-Wook, J. Hyun Suk, S. Hyunjung, P. Nam-Gyu, High-efficiency perovskite solar cells, Am. Chem. Soc. Sci. 120 (15) (2020) 7867–7918.
[18] S. Florent, W. Jérémie, K. Brett A, B. Matthias, M. Raphaël, P.-S. Bertrand, B. Loris, D. Laura, D. Juan J, Leon, S. Da vide, C. Gianluca, D. Matthieu, B. Mathieu, N. Sylvain, J. Quentin, N. Bjoern, B. Christophe, Fully textured monolithic perovskite/silicon tandem solar cells with 25.2% power conversion efficiency, Nat. Mater. 17 (2018) 820–826.
[19] A. Md Safin, M. Saiduzzaman, B. Arpon, A. Tanjun, S. Al dina, M.H. Khandaker, Tuning band gap and enhancing optical functions of $AGeF_3$ (A = K, Rb) under pressure for improved optoelectronic applications, Sci. Rep. 12 (1) (2022).
[20] C. Bo, Y. Zhengshan J, M. Salman, W. Shen, W. William, Y. Zhenhua, Y. Guang, N. Zhenyi, D. Xuezeng, H. Zachary C, H. Jinsong, Blade-coated perovskites on textured siliconfor 26%-efficient monolithic perovskite/SiliconTandem solar cells, Joule 4 (2020) 1–15.
[21] S.K. Mitro, M. Saiduzzaman, B. Arpon, S. Aldina, M.H. Khandaker, Electronic phase transition and enhanced optoelectronic performance of lead-free halide perovskites $AGeI_3$ (A = Rb, K) under pressure, Mater. Today Commun. 31 (2022).
[22] D. Saikia, M. Alam, J. Bera, A.N. Gandhi, S. Satyajit, A First-Principles Study on $ABBr_3$(A = Cs, Rb, K, Na; B = Ge, Sn) Halide Perovskites for Photovoltaic Applications, 2022 *[cond-mat.*mtrl-sci].
[23] C.J. Howard, H.T. Stokes, Structures and phase transitions in perovskites - a group-theoretical approach, Acta Crystallogr., Sect. A: Found. Crystallogr. 61 (1) (2005) 93–111.
[24] M.W. Lufaso, P.M. Woodward, Structural Science Prediction of the crystal structures of perovskites using the software program SPuDS, Acta Crystallogr., Sect. A: Found. Crystallogr. 57 (2001) 725–738.
[25] R. Tilley, Perovskites structure-property relationships, Wiley Sons LTD 1 (1) (2016) 4–5.
[26] I. Hamideddine, N. Tahiri, O.E. Bounagui, H. Ez Zahraouy, Ab initio study of structural and optical properties of the halide perovskite KBX_3 compound, J. Korean Ceram. Soc. 59 (2022) 350–358.
[27] M. Houari, B. Bouadjemi, S. Haid, M. Matougui, T. Lantri, Z. Aziz, S. Bentata, B. Bouhafs, Semiconductor behavior of halide perovskites $AGeX_3$ (A = K, Rb and Cs; X = F, Cl and Br): first-principles calculations, Indian J. Phys. 94 (4) (2020) 455–467.
[28] T. Luo, Y. Xia, J. Huang, X. Huang, Z. Wu, Y. Chen, X. Xu, W. Xie, P. Liu, C. Hu, X. Lu, T. Shi, Different structural evolutions of inorganic perovskite $CsGeI_3$, CrystEngComm 23 (28) (2021) 4917–4922.
[29] K. Thirumal, D. Hong, Y. Chen, L.W. Lin, B. Tom, Z. Ziyi, S. Matthew, L. Shuzhou, A. Mark, M. Nripan, Lead-free germanium iodide perovskite materials for photovoltaic applications, J. Mater. Chem.A 3 (47) (2015) 23829–23832.
[30] P. Giannozzi, S. Baroni, N. Bonini, M. Calandra, R. Car, C. Cavazzoni, D. Ceresoli, G.L. Chiarotti, M. Cococcioni, I. Dabo, A.D. Corso, S. Fabris, G. Fratesi, S. de Giron coli, R. Gebauer, U. Gerstmann, C. Gougoussis, A. Kokalj, M. Lazzeri, L. Martin-Samos, N. Marzari, F. Mauri, R. Maz zarello, S. Paolini, A. Pasquarello, L. Paulatto, C. Sbraccia, S. Scandolo, G. Sclauzero, A.P. Seitsonen, A. Smo gunov, P. Umari, R. M. Wentzcovitch, QUANTUM ESPRESSO: a modular and open-source software project for quantum simulations of materials, J. Phys. Condens. Matter 21 (2009), 395502.
[31] W. Kohn, L.J. Sham, Self-consistent equations including exchange and correlation effects, Phys. Rev. 140 (4A) (1965).
[32] J.P. Perdew, B. Kieron, E. Matthias, Generalized gradient approximation made simple, Phys. Rev. Lett. 77 (18) (1996) 3865–3868.
[33] H.J. Monkhorst, J.D. Pack, Special points for Brillonin zone integrations, Phys. Rev. B 12 (12) (1976) 5188–5192.

[34] M. Cristiano, D.C. Andrea, Quasi-harmonic thermoelasticity of palladium, platinum, copper, and gold from first principles, J. Phys. Condens. Matter 33 (47) (2021).
[35] O. Motornyi, N. Vast, I. Timrov, O. Baseggio, S. Baroni, A. Dal Corso, Electron energy loss spectroscopy of bulk gold with ultrasoft pseudopotentials and the Liouville Lanczos method, Phys. Rev. B 102 (3) (2020) 12.
[36] V.G. Tyuterev, V. Nathalie, Murnaghan's equation of state for the electronic ground state energy, Comput. Mater. Sci. 38 (2) (2006) 350–353.
[37] M. Robinson, M. Mwende, Ab initio study of structural, electronic, elastic, mechanical, and optical properties of K_4XP_2 (X=Zn, Cd) compounds for optoelectronic applications, Materialia 26 (2022).
[38] M. Koichi, I. Fujio, VESTA-3 for three-dimensional visualization of crystal, volumetric and morphology data, J. Appl. Crystallogr. 44 (2) (2011) 1272–1276.
[39] S. Wahyu, C. Stefano, High-throughput electronic band structure calculations: challenges and tools, Comput. Mater. Sci. 49 (2) (2010) 299–312.
[40] M. Mwende, M. George S, M. Robinson J, *Ab ini tio* study of $K_3Cu_3P_2$ material for photovoltaic applications, Computational Condensed Matter 32 (2022).
[41] M. Félix, C.F. Xavier, Necessary and sufficient elastic stability conditions in various crystal systems, Phys. Rev. B 90 (22) (2014), 224104.
[42] Q. Liu, H. Qin, Z. Jiao, F.S. Liu, Z.T. Liu, First principles calculations of structural, elastic, and electronic properties of trigonal $ZnSnO_3$ under pressure, Mater. Chem. Phys. 180 (2016) 75–81.
[43] V. Woldeman, Lehrbuch der Kristallphysik, vol. XXIV, mit Ausschluss der Kristalloptik, 1910.
[44] K. Shiferaw, M.W. Menberu, Structural, electronic, lattice dynamic, and elastic properties of $SnTiO_3$ and $PbTiO_3$ using density functional theory, Adv. Condens. Matter Phys. 2019 (2019) 13.
[45] A. Reuss, Berechnung der Fließgrenze von Mischkristallen auf Grund der Plastizitätsbedingung für Einkristalle, ZAMM—Zeitschrift f ur Angewandte Mathematik und Mechanik 9 (1) (1929) 49–58.
[46] R. Hill, The elastic behavior of a crystalline aggregate, Proc. Phys. Soc. 65 (1952) 349–354.
[47] H. Dong, C. Chen, S. Wang, W. Duan, J. Li, Elastic properties of tetragonal $BiFeO_3$ from first-principles calculations, Appl. Phys. Lett. 102 (18) (2013).
[48] M. Mwende, M. Robinson J, First-principle calculations to investigate structural, electronic, elastic, mechanical, and optical properties of K_2CuX (X=As, Sb) ternary compounds, Adv. Mater. Sci. Eng. (2022) 1–10.
[49] S. Mitro, K. Hossain, R. Majumder, H. Md Zahid, Effect of the negative chemical pressure on physical properties of doped perovskite molybdates in the framework of DFT method, J. Alloys Compd. 854 (2021).
[50] M.H.K. Rubel, S. Mitro, B. Mondal, M. Rahaman, M. Saiduzzaman, J. Hossain, A. Islam, N. Kumada, Newly synthesized A-site ordered cubic-perovskite super conductor $(Ba_{0.54}K_{0.46})_4Bi_4O_{12}$: a DFT investigation, Physica C: Superconductivity and its Applications 574 (2020).
[51] A. Sikander, I. Muhammad, A. Zeesham, R. Malika, S. Tahira, Y. Ayesha, A. Naseem, L. Bushra, S. Muhammad, A.-S. Abdullah G, DFT study of the electronic and optical properties of ternary chalcogenides AlX_2Te_4, Mater. Res. Express 6 (2019), 116314.
[52] M. Benchehima, H. Abid, A. Sadoun, C. Chabane, Optoelectronic properties of aluminum bismuth antimony ternary alloys for optical telecommunication applications: first principles calculation, Comput. Mater. Sci. 155 (2018) 224–234.
[53] M.G. Hamid, A.A. Zeyad, M.H.Q. Saif, H. Mahmoud, S.A. Abdullah, Density functional study of cubic, tetragonal, and orthorhombic $CsPbBr_3$ perovskite, ACS Omega 5 (13) (2020) 7468–7480.